Numerical and experimental validation of a three-dimensional combustion diagnostic based on tomographic chemiluminescence

Weiwei Cai,[1] Xuesong Li,[1] Fei Li,[2] and Lin Ma[1,*]

[1]*Department of Aerospace and Ocean Engineering, Virginia Tech, Blacksburg, VA 24061, USA*
[2]*State Key Lab of High Temperature Gas Dynamics, Institute of Mechanics, Chinese Academy of Sciences, Beijing 100190, China*
**LinMa@vt.edu*

Abstract: Three-dimensional (3D) measurements are highly desirable both for fundamental combustion research and practical monitoring and control of combustion systems. This work discusses a 3D diagnostic based on tomographic chemiluminescence (TC) to address this measurement need. The major contributions of this work are threefold. First, a hybrid algorithm is developed to solve the 3D TC problem. The algorithm was demonstrated in extensive tests, both numerical and experimental, to yield 3D reconstruction with high fidelity. Second, an experimental approach was designed to enable quantifiable metrics for examining key aspects of the 3D TC technique, including its spatial resolution and reconstruction accuracy. Third, based on the reconstruction algorithm and experimental results, we investigated the effects of the view orientations. The results suggested that for an unknown flame, it is better to use projections measured from random orientations than restricted orientations (e.g., coplanar orientations). These findings are expected to provide insights to the fundamental capabilities of the TC technique, and also to facilitate its practical application.

OCIS codes: (280.1740) Combustion diagnostics; (100.6890) Three-dimensional image processing; (120.0280) Remote sensing and sensors.

References and links

1. K. Kohse-Hoinghaus and J. B. Jeffries, *Applied Combustion Diagnostics* (Taylor & Francis, 2002).
2. A. C. Eckbreth, *Laser Diagnostics for Combustion Temperature and Species* (Gordon and Breach Publishers, 1996).
3. Y. Hardalupas, C. S. Panoutsos, and A. M. K. P. Taylor, "Spatial resolution of a chemiluminescence sensor for local heat-release rate and equivalence ratio measurements in a model gas turbine combustor," Exp. Fluids **49**(4), 883–909 (2010).
4. M. Orain and Y. Hardalupas, "Measurements of local mixture fraction of reacting mixture in swirl-stabilised natural gas-fuelled burners," Appl. Phys. B **105**(2), 435–449 (2011).
5. Y. Hardalupas, M. Orain, C. S. Panoutsos, A. M. K. P. Taylor, J. Olofsson, H. Seyfried, M. Richter, J. Hult, M. Aldén, F. Hermann, and J. Klingmann, "Chemiluminescence sensor for local equivalence ratio of reacting mixtures of fuel and air (FLAMESEEK)," Appl. Therm. Eng. **24**(11-12), 1619–1632 (2004).
6. Y. Zhao, C. Tong, and L. Ma, "Demonstration of a new laser diagnostic based on photodissociation spectroscopy for imaging mixture fraction in a non-premixed jet flame," Appl. Spectrosc. **64**(4), 377–383 (2010).
7. J. A. Sutton and J. F. Driscoll, "A method to simultaneously image two-dimensional mixture fraction, scalar dissipation rate, temperature and fuel consumption rate fields in a turbulent non-premixed jet flame," Exp. Fluids **41**(4), 603–627 (2006).
8. B. O. Ayoolan, R. Balachandran, J. H. Frank, E. Mastorakos, and C. F. Kaminski, "Spatially resolved heat release rate measurements in turbulent premixed flames," Combust. Flame **144**(1-2), 1–16 (2006).
9. S. Bockle, J. Kazenwadel, T. Kunzelmann, D. I. Shin, C. Schulz, and J. Wolfrum, "Simultaneous single-shot laser-based imaging of formaldehyde, OH, and temperature in turbulent flames," Proc. Combust. Inst. **28**(1), 279–286 (2000).
10. N. Anikin, R. Suntz, and H. Bockhorn, "Tomographic reconstruction of the OH* chemiluminescence distribution in premixed and diffusion flames," Appl. Phys. B **100**(3), 675–694 (2010).
11. Y. Ikeda, J. Kojima, and H. Hashimoto, "Local chemiluminescence spectra measurements in a high-pressure laminar methane/air premixed flame," Proc. Combust. Inst. **29**(2), 1495–1501 (2002).

#175611 - $15.00 USD Received 5 Sep 2012; revised 1 Nov 2012; accepted 1 Jan 2013; published 13 Mar 2013

12. J. Kojima, Y. Ikeda, and T. Nakajima, "Basic aspects of OH(A), CH(A), and C_2(d) chemiluminescence in the reaction zone of laminar methane-air premixed flames," Combust. Flame **140**(1-2), 34–45 (2005).
13. H. N. Najm, P. H. Paul, C. J. Mueller, and P. S. Wyckoff, "On the adequacy of certain experimental observables as measurements of flame burning rate," Combust. Flame **113**(3), 312–332 (1998).
14. K. Nakabe, Y. Mizutani, T. Hirao, and H. Fujioka, "An experimental study on detailed flame structure of liquid fuel sprays with and without gaseous fuel," Combust. Flame **84**(1-2), 3–14 (1991).
15. J. Kojima, Y. Ikeda, and T. Nakajima, "Spatially resolved measurement of OH*, CH*, and C_2* chemiluminescence in the reaction zone of laminar methane/air premixed flames," Proc. Combust. Inst. **28**(2), 1757–1764 (2000).
16. Y. Hardalupas and M. Orain, "Local measurements of the time-dependent heat release rate and equivalence ratio using chemiluminescent emission from a flame," Combust. Flame **139**(3), 188–207 (2004).
17. J. Kojima, Y. Ikeda, and T. Nakajima, "Spatially resolved measurement of OH*, CH*, and C_2* chemiluminescence in the reaction zone of laminar methane/air premixed flames," Proc. Combust. Inst. **28**(2), 1757–1764 (2000).
18. L. A. Feldkamp, L. C. Davis, and J. W. Kress, "Practical cone-beam algorithm," J. Opt. Soc. Am. A **1**(6), 612–619 (1984).
19. G. W. Faris and R. L. Byer, "Beam-deflection optical tomography of a flame," Opt. Lett. **12**(3), 155–157 (1987).
20. Y. Ishino and N. Ohiwa, "Three-dimensional computerized tomographic reconstruction of instantaneous distribution of chemiluminescence of a turbulent premixed flame," JSME Int. J. Ser. B **48**(1), 34–40 (2005).
21. N. Anikin, R. Suntz, and H. Bockhorn, "Tomographic reconstruction of the OH*-chemiluminescence distribution in premixed and diffusion flames," Appl. Phys. B-Lasers and Opt. **100**(3), 675–694 (2010).
22. M. M. Hossain, G. Lu, and Y. Yan, "Optical fiber imaging based tomographic reconstruction of burner flames," IEEE Trans. Instrum. Meas. **61**(5), 1417–1425 (2012).
23. J. Floyd and A. M. Kempf, "Computed tomography of chemiluminescence (CTC): high resolution and instantaneous 3D measurements of a matrix burner," Proc. Combust. Inst. **33**(1), 751–758 (2011).
24. C. T. Herman, *Image Reconstruction from Projections - The Fundamentals of Computerized Tomography* (Academic Press, 1980).
25. X. An, T. Kraetschmer, K. Takami, S. T. Sanders, L. Ma, W. Cai, X. Li, S. Roy, and J. R. Gord, "Validation of temperature imaging by H_2O absorption spectroscopy using hyperspectral tomography in controlled experiments," Appl. Opt. **50**(4), A29–A37 (2011).
26. L. Ma, W. Cai, A. W. Caswell, T. Kraetschmer, S. T. Sanders, S. Roy, and J. R. Gord, "Tomographic imaging of temperature and chemical species based on hyperspectral absorption spectroscopy," Opt. Express **17**(10), 8602–8613 (2009).
27. Q. Huang, F. Wang, J. Yan, and Y. Chi, "Simultaneous estimation of the 3D soot temperature and volume fraction distributions in asymmetric flames using high-speed stereoscopic images," Appl. Opt. **51**(15), 2968–2978 (2012).
28. L. Ma and W. Cai, "Numerical investigation of hyperspectral tomography for simultaneous temperature and concentration imaging," Appl. Opt. **47**(21), 3751–3759 (2008).
29. L. Ma and W. Cai, "Determination of the optimal regularization parameters in hyperspectral tomography," Appl. Opt. **47**(23), 4186–4192 (2008).
30. E. Y. Sidky, C. M. Kao, and X. H. Pan, "Accurate image reconstruction from few-views and limited-angle data in divergent-beam CT," J. XRay Sci. Technol. **14**, 119–139 (2006).
31. W. H. Press, S. A. Teukolsky, W. T. Vetterling, and B. P. Flannery, *Numerical Recipes in FORTRAN: The Art of Scientific Computing* (Cambridge University Press, 1992).
32. R. Crowther, D. DeRosier, and A. Klug, "The reconstruction of a three-dimensional structure from projections and its application to electron microscopy," Proc. R. Soc. Lond. A Math. Phys. Sci. **317**(1530), 319–340 (1970).
33. H. M. Hudson and R. S. Larkin, "Accelerated image reconstruction using ordered subsets of projection data," IEEE Trans. Med. Imaging **13**(4), 601–609 (1994).
34. W. Cai, D. J. Ewing, and L. Ma, "Investigation of temperature parallel simulated annealing for optimizing continuous functions with application to hyperspectral tomography," Appl. Math. Comput. **217**(12), 5754–5767 (2011).
35. W. Cai and L. Ma, "Hyperspectral tomography based on proper orthogonal decomposition as motivated by imaging diagnostics of unsteady reactive flows," Appl. Opt. **49**(4), 601–610 (2010).
36. D. S. Nobes, B. Wieneke, and R. P. Tatam, "Determination of view vectors from image warping mapping functions," Opt. Eng. **43**(2), 407–414 (2004).

1. Introduction

Chemiluminescence from combustion radicals (e.g., OH*, CH*, CO_2*, and C_2*) represents a unique diagnostic opportunity in reactive flows, both for fundamental study and practical deployment. Diagnostics based on chemiluminescence can be substantially simpler and easier to implement than other optical diagnostics, yet provide measurements which are otherwise challenging to obtain. Most combustion diagnostics require laser sources and/or external seeding, which are usually costly, cumbersome, or even infeasible [1, 2]. In contrast, diagnostics based on chemiluminescence bypass such requirements since chemiluminescence is emitted naturally in combustion processes. In spite of the simplicity, chemiluminescence

#175611 - $15.00 USD Received 5 Sep 2012; revised 1 Nov 2012; accepted 1 Jan 2013; published 13 Mar 2013

provides information about key combustion quantities which are challenging to obtain, with the rate of heat release and local equivalence ratio being two notable examples. Both quantities are critical for the fundamental understanding of combustion instability, a phenomenon that can lead to reduced efficiency or even the destruction of gas turbines and aero-propulsion systems [3].

Here, we briefly review common techniques from our perspective to motivate chemiluminescence-based techniques. Existing techniques for the measurement of local equivalent ratio are typically based on 1) laser induced fluorescence (LIF) to track a fuel marker [2, 3], 2) Raman scattering to measure fuel concentration [2, 3], or 3) chemiluminescence from two combustion radicals (e.g., OH* and CH*) [3–5]. All three types of techniques have been relatively well-established, and have become standard diagnostic tools for combustion research. Both LIF and Raman techniques require high power lasers. The fuel marker introduced may not faithfully track the fuel vapor due to its different physical and chemical properties than the fuel vapor [1, 6, 7]. Furthermore, the quantification of LIF signal is complicated due to specie- and temperature-dependent quenching rates. Application of Raman techniques is restricted to "clean" environment (free from particulates, soot, and background luminosity) due to the relative low signal level of Raman scattering [1, 2]. For the rate of heat release, existing techniques are typically based on 1) LIF measurements of two species which are the reactants of a reaction whose rate correlates with rate of heat release [8, 9], and 2) chemiluminescence measurements of radicals (typically OH* and CH*) whose concentration correlate with rate of heat release [5, 10]. The simultaneous LIF measurements of two flame species again require high power lasers, and the quantitative interpretation of LIF measurements is non-trivial due to species- and temperature-dependent quenching rates.

The above discussion motivates the consideration of chemiluminescence for measuring local equivalence ratio and rate of heat release. Compared to LIF- or Raman-based techniques, chemiluminescence does not require laser sources and the interpretation of signal is relatively straightforward. These advantages significantly simplify the alignment and implementation, and are especially appealing for application in practical systems.

The limitations of chemiluminescence-based techniques have also been well recognized. Chemiluminescence signal is also difficult to quantity and its applicable range has been extensively investigated in terms of temperature, pressure, equivalence ratio, and strain rate [3, 5, 11–13]. Out of all the limitations, the lack of spatial resolution perhaps represents the most important limitation of chemiluminescence-based techniques.

Therefore, this work addresses the issue of spatial resolution of chemiluminescence-based techniques. Chemiluminescence is naturally emitted from the entire volume of combustion zones, resulting in its line-of-sight averaged nature. In contrast, LIF- or Raman-based techniques utilize signals artificially generated by laser illumination, and the illumination volume provides well-defined spatial resolution. Since spatially resolved measurements are highly desired for model validation and development, research efforts have been invested by several groups to achieve spatial-resolved chemiluminescence measurements. These efforts can be broadly divided into two approaches.

The first approach approximates point-measurement of chemiluminescence by designing the collection system so that only the chemiluminescence emitted from a well-defined and relatively small volume is collected to the detector. This approach seems to originate from an intrusive probe first demonstrated in 1991 [14]. Non-intrusive implementations subsequently have been demonstrated using Cassegrain telescope optics [3–5, 11, 15, 16]. These implementations have achieved nominal spatial resolution on the order of 100-200 μm in diameter and 800-1600 μm in length [3, 17]. Extension of this pointwise approach to multiple dimension measurement could be accomplished by scanning the probe if the target flame is steady, or by employing multiple probes simultaneously.

The second approach involves combining chemiluminescence with tomography to obtain spatially-resolved measurements in two-dimensional (2D) or 3D. Compared to the above pointwise approach, the tomographic chemiluminescence (TC) approach can provide 2D or 3D measurements directly (i.e., without scanning), thusly providing valuable or even critical

#175611 - $15.00 USD Received 5 Sep 2012; revised 1 Nov 2012; accepted 1 Jan 2013; published 13 Mar 2013

structural information of turbulent flames. Early efforts, limited by hardware, typically relied on sequentially recorded projections or a few number of simultaneously projections to obtain 2D measurements [18, 19]. Recent advancements in digital cameras, fiber optics, and computing technologies have provided the opportunity to simultaneously record projections from a relatively large number of view angles at high speed (thusly enabling high temporal resolution also), and subsequently process the projections via tomographic reconstruction to obtain 3D measurements. For instance, a customized camera with multiple lenses was reported in 2005 to capture projections from 40 view angles, based on which 3D tomographic reconstructions were performed to obtain 3D flame structure at 500 frame per second (fps) [20]. Similar implementation of this multi-lens camera system can also be realized using image fibers, as reported more recently [21, 22], to collect multiple projections to the same camera. Alternatively, multiple cameras can also be used to collect multiple projections [23], an attractive option given the increasingly affordable consumer/industrial cameras. These past efforts have demonstrated TC's potential for 3D measurement with sub-millimeter spatial resolution and temporal resolution on the order of tens of microsecond, representing diagnostics capabilities solely needed.

This work focuses on obtaining 3D measurements using tomographic chemiluminescence. More specifically, based on the past work reviewed above, this work 1) investigated 3D reconstruction algorithms and the use of regularization, 2) demonstrated an experimental approach to examine the performance of the 3D TC technique quantitatively, and 3) investigated the potential advantages of using projections from arbitrary view angles. In the next two sections, Sections 2 and 3, we first introduce the mathematical formulation of the 3D TC problem and the inversion algorithm, which is numerically validated in Section 4. Sections 5 and 6 describe the experimental approach and demonstration of the 3D TC technique. Based on these numerical and experimental results, Section 7 discusses the effects of view orientations on the reconstruction. Finally, Section 8 summarizes the paper.

2. Mathematical formulation

Figure 1 illustrates the mathematical formulation of the TC problem. Here we use *F(x,y,z)* to denote the 3D distribution of the chemiluminescence emission to be measured, which is proportional to the concentration of the radicals that emit the chemiluminescence (e.g., CH* or OH*). To perform tomography computationally, F is discretized into voxels in a Cartesian coordinate system (x-y-z) as shown. An imaging system records the 2D images of F on a camera (a CCD array in this work), and the image formed on the CCD array depends on its relative distance and orientation, specified by r (distance), θ (azimuth angle), and ϕ (inclination angle). Once the components in the imaging system (i.e., specifications of the lenses) are fixed, the image formed on the CCD array is uniquely determined by F, r, θ, and ϕ. We call the 2D images recorded on the CCD array *projections*, denoted as $P(r, \theta, \phi)$. The relationship between P and F is:

$$P(r,\theta,\phi) = \sum_{i_x}\sum_{i_y}\sum_{i_z} F(x_i, y_i, z_i) \cdot PSF(x_i, y_i, z_i; r, \theta, \phi) \tag{1}$$

where i_x, i_y, i_z are the indices of the voxel centered at (x_i, y_i, z_i); and *PSF* is the *point spread function* defined as the projection formed by a point-source located at (x_i, y_i, z_i) with unity intensity. Physically, Eq. (1) states that the projection is a weighted summation of the *PSF* across all voxels, and the weights are the value of the sought distribution. Now the 3D TC problem can be formally formulated as:

Given a set of projections (Ps) measured at various distances and orientations, find *F(x,y,z)*.

#175611 - $15.00 USD Received 5 Sep 2012; revised 1 Nov 2012; accepted 1 Jan 2013; published 13 Mar 2013

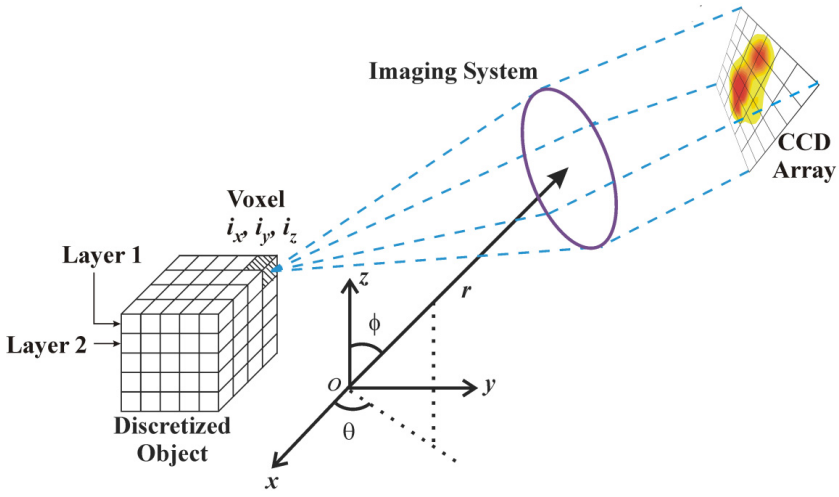

Fig. 1. Illustration of the mathematical formulation of volumetric tomographic.

The *PSF* does not depend on the sought *F*. Therefore computationally, the *PSFs* are pre-calculated for the measurement locations and orientations (defined by *r, θ,* and *ϕ*). However, the *PSF* requires relatively large memory due to the 3D nature of the problem. The size of the *PSF* depends (almost linearly) on the degree of discretization of *F* and the projection, i.e., the number of effective pixels on which a projection is recorded and resolved. In our work, with *F* discretized into 30 × 30 × 30 voxels and the projections recorded on ~1.6 × 10^5 pixels (a 400 × 400 CCD array), the *PSF* at each view angle required more than 2 GB of memory. Similar memory demands were also reported in [23]. Strategies to mitigate such memory demand will be discussed in a separate publication, so that this current paper stays focused on the fundamental issues of solving the 3D TC problem.

3. Tomographic inversion algorithm and regularization

Various algorithms have been developed to solve the tomographic inversion problem as formulated above [18, 24]. In our opinion, a systematic comparison of these algorithms, which admittedly is a tremendous endeavor and is beyond the scope of this work, will be highly valuable for a wide spectrum of applications. This work developed a hybrid algorithm combining ART (Algebraic Reconstruction Technique) and minimization technique, in which the ART algorithm was used to provide an initial guess for the minimization algorithm. This hybrid algorithm is motivated by the following two observations made from previous tomography work under the context of combustion diagnostics, both from our own and other research groups.

First, combustion applications, due to optical access and the dynamic nature combustion processes, typically have limited number of projections available, ranges from 2 [25, 26] to about 50 [20–23, 27]. In contrast, other applications (e.g., medical imaging) have significantly more projections (thousands and more) available. Well-established (and also mathematically exact) algorithms such as filtered back projection and Fourier reconstruction [24] do not work optimally with such limited projections available in combustion diagnostics. With the limited projections in combustion diagnostics, past results suggest that inversion method based on minimization can solve the tomography problem effectively in the presence of measurement noises [21, 26–29]. The tomography problem is cast into the following minimization problem:

$$\min \sum_{r,\theta,\phi} [P_m(r,\theta,\phi) - P_c(r,\theta,\phi)]^2 \text{ with respect to } F(x,y,z) \tag{2}$$

where P_m represents the measured projections at (r, θ, ϕ), P_c the projection calculated at (r, θ, ϕ) with a given distribution according to Eq. (1), and the summation runs over all locations

#175611 - $15.00 USD Received 5 Sep 2012; revised 1 Nov 2012; accepted 1 Jan 2013; published 13 Mar 2013

and orientations of measurements. Equation (2) essentially seeks the F that best (in the least squares sense) reproduces the projection measurements.

Second, certain properties of the sought distribution F are often known *a priori* in combustion diagnostics. For instance, the concentrations of radicals are nonnegative and bounded within a certain range, and the distribution is smooth due to heat and mass transfer. Therefore it is desirable to have an algorithm that can incorporate such *a priori* information when available to improve the reconstruction fidelity. The minimization technique described in Eq. (2) allows the flexible incorporation of *a priori* information via regularization. As shown below, instead of only minimizing the difference between measured and calculated projections as shown in Eq. (2), a regularization term (R) can be added:

$$\min \sum_{r,\theta,\phi} [P_m(r,\theta,\phi) - P_c(r,\theta,\phi)]^2 + \gamma \times R(F) \text{ with respect to } F(x,y,z) \tag{3}$$

The regularization term is a function of F, and various mathematical expressions can be developed to quantify different types of *a priori* information of F [29, 30]. The regularization parameter, γ, is a preset constant that balances the relative weights of the first term and the regularization term [31]. In this work, γ was chosen using the guidelines provided in [31], and the optimal choice of γ is a nontrivial topic that deserves a seperate treatment. Incorporation of *a priori* information via regularization has been demonstrated effective to ameliorate the ill-posedness of the inversion problem due to limited projection data [30, 31].

These observations were confirmed by extensive numerical simulations for the TC problems. Some of these results are shown in Fig. 2 to Fig. 4 using various phantoms and variations of different algorithms, including ART as described in [23], our hybrid algorithm, MART (Multiplicative Algebraic Reconstruction Technique) as described in [32], and OSEM (Ordered Subset Expectation Maximization) as described in [33].

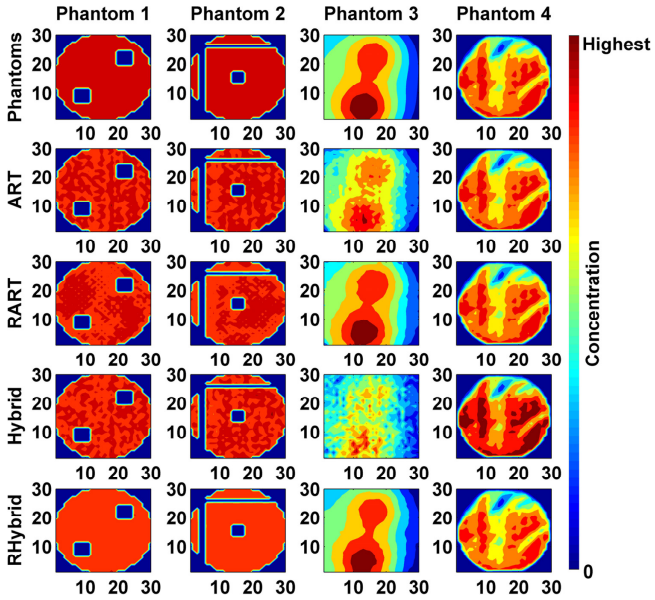

Fig. 2. Comparison of phantoms and reconstructions.

The top row of Fig. 2 shows four of the phantoms tested in our numerical simulations. The four phantoms shown in Fig. 2 include (from left to right) 1) a circular and uniform distribution with two square regions having zero value (The color scale is such that dark red and dark blue, respectively, indicates highest and zero concentration of the target radical. The same color scale is used hereafter), 2) a circular and uniform distribution with a square region and two lines with different thickness having zero value, 3) a smooth and continuous distribution with two peaks, and 4) a CH* distribution obtained by simulating a turbulent

#175611 - $15.00 USD Received 5 Sep 2012; revised 1 Nov 2012; accepted 1 Jan 2013; published 13 Mar 2013

opposed-flow flame. All phantoms are discretized into 30 × 30 × 30 voxels. Figure 2 shows the fifteenth layer of the distribution. For phantoms 1, 2, and 3, the distribution is the same (as shown in the top row) on all layers to facilitate visualization; and for phantom 4, the distribution varies from layer to layer to simulate a turbulent flame. Phantoms 1 and 2 are created to simulate the flames experimentally tested, as detailed in Section 5.

Rows 2 through 5 in Fig. 2 show the reconstruction obtained using ART and the hybrid algorithm, with and without regularization on the fifteen's layer. Results obtained with regularization are labeled as RHybrid and RART (regularized-Hybrid and -ART). Figure 3 shows the overall reconstruction error across all layers as defined by:

$$e = \frac{\sum_{i_x}\sum_{i_y}\sum_{i_z}\left|F^{rec}_{i_x,i_y,i_z} - F_{i_x,i_y,i_z}\right|}{\sum_{i_x}\sum_{i_y}\sum_{i_z}\left|F_{i_x,i_y,i_z}\right|} \tag{4}$$

where F^{Rec} represents the reconstructed distribution of the target radical.

These results were obtained using projections measured from 8 view angles randomly chosen (but once chosen, these view angles were used in all algorithms to make the results comparable). To simulate practical conditions in our experiments, a 5% Gaussian noise was artificially added to the projections in these simulations. All algorithms were terminated when the relative change between two consecutive iterations was less than 10^{-3}.

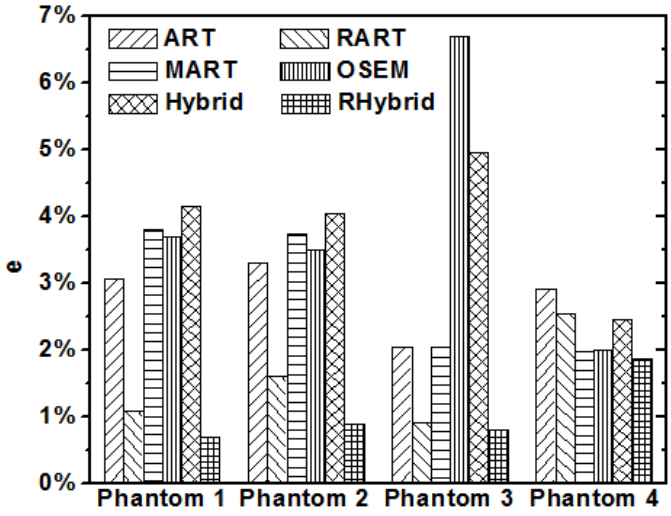

Fig. 3. Comparison of overall reconstruction error using different algorithms.

There are multiple criteria that can be used to quantify the reconstruction fidelity across algorithms other than the overall *e* defined in Eq. (4). For example, the correlation between the phantoms and reconstructions can also be used to quantify the reconstruction fidelity [23]. In all our tests, the RHybrid algorithms also outperformed other algorithms under the correlation criterion. Figure 4 examines the reconstruction fidelity by another criterion: the distribution of reconstructions on each voxel. Both the overall *e* as shown in Fig. 3 and the correlation criterion essentially averages the reconstruction error among all voxels in the measurement domain. However, the flame may not exist in all voxels and hence can bias both criteria. Therefore, Fig. 4 provides a detailed illustration of the reconstruction error. Here the error is defined as the absolute value of reconstruction discrepancy at each voxel, normalized by the maximum value of sought function over the measurement of interest. As Fig. 4 shows, both the RART and RHybrid algorithm improved the reconstruction fidelity within the flame

#175611 - $15.00 USD Received 5 Sep 2012; revised 1 Nov 2012; accepted 1 Jan 2013; published 13 Mar 2013

zone, and the RHybrid algorithm did not only reduce the overall *e* as shown in Fig. 3 but also the peak error.

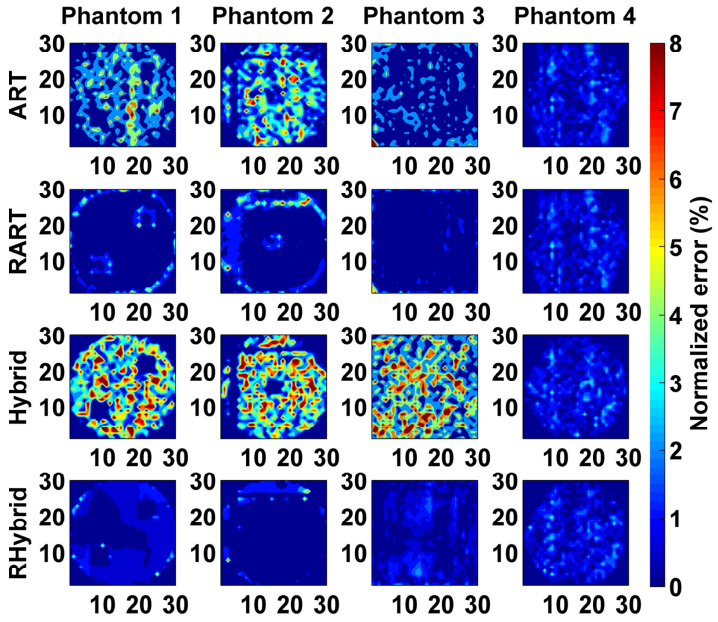

Fig. 4. Distribution of reconstruction errors for phantoms shown in Fig. 2.

As seen from Fig. 2 to Fig. 4, both ART and the hybrid algorithm can reconstruct all phantoms with reasonable fidelity, and the application of regularization significantly improved the fidelity. In all our numerical tests, the RHybrid algorithm yielded best reconstructions with smallest *e*, and was chosen for the rest of the work. The regularization used here is a so-called total variation (TV) regularization as described in [30]. The TV of the target function *F* is defined as:

$$R_{TV}(F) = \sum_{i_x,i_y,i_z} \sqrt{(F_{i_x,i_y,i_z} - F_{i_x-1,i_y,i_z})^2 + (F_{i_x,i_y,i_z} - F_{i_x,i_y-1,i_z})^2 + (F_{i_x,i_y,i_z} - F_{i_x,i_y,i_z-1})^2} \qquad (5)$$

According to Eq. (5), the *TV* of *F* represents the summation of the gradient magnitude of *F* over all voxels. Inclusion of R_{TV} in the reconstruction can preserve the smoothness or the edges of the sought *F* [30]. Therefore, as expected, the improvement was more dramatic on phantoms 1-3 than phantom 4, because phantoms 1 and 2 have clear edges and phantom 3 is smooth and continuous. In the RHybrid algorithm, the R_{TV} term as described in Eq. (5) is simply used in Eq. (3). In the RART algorithm, the R_{TV} term is minimized at the end of each ART iteration with respect to *F*, and the updated *F* is used as the input for the next ART iteration. Note that in this approach, the regularization and the ART iteration (which minimizes the difference between the calculated projections and the measurements) are essentially performed separately. Whereas in contrast, the RHybrid algorithm considers the regularization and the minimization of the difference between calculated and measured projections simultaneously (or holistically). We believe this contributes to the smaller *e* obtained by the RHybrid than the RART algorithm.

4. Numerical verification

Extensive numerical simulations have been conducted to verify the use of the RHybrid algorithm using various phantoms and noises. Figure 5 summarizes the results obtained on phantom 2 and 4 shown in Fig. 2, with phantom 2 representing one of the experimental flames tested in this work and phantom 4 a turbulent flame. These simulations were

#175611 - $15.00 USD Received 5 Sep 2012; revised 1 Nov 2012; accepted 1 Jan 2013; published 13 Mar 2013

performed under various noise levels, ranging from 0% to 10%, intended to encompass the range of noise expected in practical measurements. The experimental noise in this work is estimated to be about 5%. These results were obtained under similar configurations as those used in Fig. 2 to Fig. 4. Specifically, 8 projection measurements from 8 randomly chosen orientations were used in the reconstruction. But again, once chosen, these view angles were used in both the RART and RHybrid algorithms to make the results comparable.

As seen from Fig. 5, the RHybrid algorithm consistently outperformed the RART algorithm in terms of the overall reconstruction error for all phantoms tested at all noise levels. Based on these numerical verifications, the RHybrid algorithm was chosen to process the data obtained in this work. We have also processed the experimental results shown in Section 6 and examined the effects of view angles shown in Section 7 using other inversion algorithms, and the trend of the results obtained agreed with those obtained by the RHybrid algorithm as reported in Section 5 and 6.

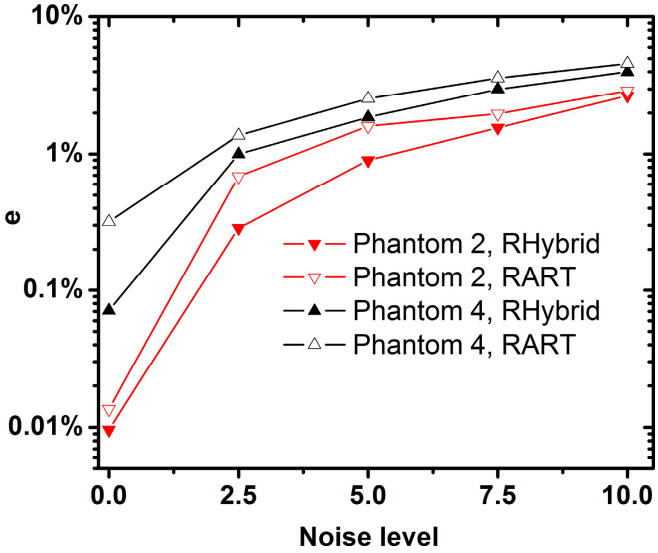

Fig. 5. Comparison of RHybrid and RART at various noise levels.

Before leaving this section and proceeding to the experiments, note that 1) with accurate projections measurements (e.g., with noise level less than 2.5%), both the RART and RHybrid algorithms can provide reconstructions with high fidelity, and 2) in this work, the lower *e* from the RHybrid algorithm was achieved at a significantly higher computational cost (more than 10 ×) than the RART algorithm. This work solved Eq. (3) using a simulated annealing (SA) algorithm [31]. The SA algorithm is well recognized for its ability to minimize complicated functions. However, the SA algorithm is a stochastic algorithm and suffers from high computational cost, and we have been exploring possible approaches to reduce the computational cost of solving Eq. (3). Possible approaches include parallelizing the SA algorithm [34], combining SA with proper orthogonal decomposition to reduce the dimension of the problem [35], or finding a deterministic algorithm to replace the SA algorithm.

5. Experimental arrangement

The TC technique was demonstrated using the experimental setup shown in Fig. 6. The setup was designed to create flames with controlled patterns so that the TC technique can be validated experimentally. The setup used a McKenna burner (illustrated in panels (a) and (b)) to produce a stable and disk-like flame with a diameter of ~61 mm and a thickness of ~1 mm. Photos of a sample flame taken from the side and top are shown in panels (c) and (d). The fuel used in this study is methane (CH_4) and the oxidizer is air. To create asymmetric flame to

#175611 - $15.00 USD Received 5 Sep 2012; revised 1 Nov 2012; accepted 1 Jan 2013; published 13 Mar 2013

demonstrate the 3D nature of TC technique, a honeycomb was place on the burner (panel (a)). The honeycomb's cells are squares with size of 1.25 × 1.25 mm (panel (b)) and certain cells were blocked to create the desired asymmetric pattern. Various patterns have been created and studied in this work. For example, phantom 1 shown in Fig. 2 illustrates one of the patterns created by blocking two rectangular regions of the honeycomb. Panel (b) of Fig. 6 here shows another pattern, where we block a rectangular region with a size of 8.75 × 10 mm, a column of cells to form a vertical line with 1.25 mm thickness, and two rows of cells to form a horizontal line with and 2.5 mm thickness. Phantom 2 shown in Fig. 2 simulates this flame.

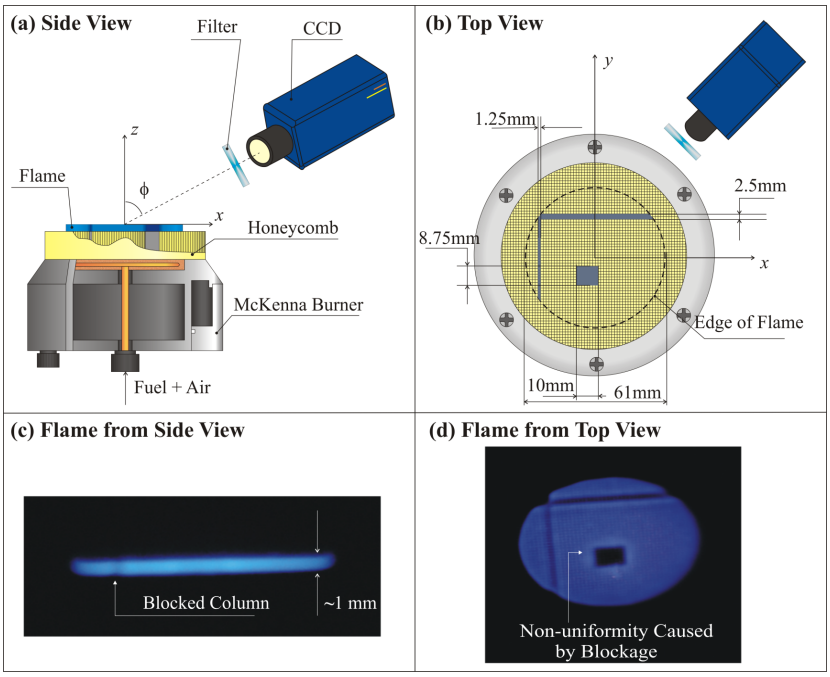

Fig. 6. Experimental setup for demonstrating the TC technique.

A CCD camera (PCO Sensicam) was used to take projection measurements of the chemiluminescence emitted from CH* radicals in the flame from various view angles sequentially. The camera was installed on a rotation stage (Newport 481-A), which was used to set the desired pitch angles. The stage was then fixed on an optical rail to adjust r's and θ's. The lens used has a focal length of 35 mm and the numerical aperture was set at 1.7 during the measurements. A band pass filter (Thorlabs MF434-17, 434 ± 8.5 nm) was applied to block the background luminosity. Each projection measurement was taken with a 50 ms exposure time. Simultaneous measurement from multiple view angles can be achieved using multiple cameras as demonstrated elsewhere [23]. The exposure time can be shortened using a different camera or different image systems. For example, in our test, an intensified CMOS camera (Photron Fastcam SA4) reduced the exposure time to tens of μs with good signal to noise ratio.

In this work, we decided to use one CCD camera to take the projection measurements sequentially at a relatively lower temporal resolution to study several fundamental aspects of the TC technique, such as the tomographic algorithm, the placement of the view angles, and spatial resolution. Other aspects of the TC technique, such as signal level and temporal resolution, will be discussed in a separate publication. Using one camera instead of multiple cameras eliminates the uncertainty caused by calibration across cameras, and CCD cameras provide better linearity than CMOS cameras. The sequential measurements with 50 ms exposure time is justified by the stability of the flame, which was measured to be stable

#175611 - $15.00 USD Received 5 Sep 2012; revised 1 Nov 2012; accepted 1 Jan 2013; published 13 Mar 2013

within 4% both in the short term (~50 ms) and long term (~10 minutes, the time needed to measure a complete set of projections). The stability of the flame represents the major uncertainty in the projections, which is the reason that results shown in Fig. 2 to Fig. 4 were obtained with 5% artificial noise.

As mentioned before, the purpose of this setup is to create controlled flame patterns. These patterns will be binary under ideal conditions, i.e., if the flame is perfectly uniform and blocked area creates a step change of the concentration of target radical (CH* in this work). However, such an ideal binary patterns were only approximated in our experiments due to convection, diffusion, and disturbance of the flow caused by the blockage. These non-ideal conditions are manifested in panels (c) and (d). For instance, if the flame pattern is perfectly binary, then the blocked column should be a completely dark region when viewed from the side as shown in panel (c). In practice, this region was darker (i.e., with lower CH* concentration) relative to other regions, but not completely dark (i.e., with zero CH* concentration). Also, the edges of the block region are not ideally sharp and uniform. As seen from panel (d), the blockage increases the flow rate in the adjacent cells and creates a non-uniform distribution in that region.

Despite of these above non-ideal features, the flames created via this approach still provide us with well-controlled patterns, and it is highly desirable to have such experimental "phantoms" to quantitatively validate the TC technique. The quantitative value of these experimental phantoms will be further elucidated later when we report the tomographic results.

6. Experimental results

Projection measurements were performed on flames created using the setup shown in Fig. 6 from various view angles. Eight of these view angles are listed in Table 1. The orientation (θ and ϕ) and location (r) of the projection measurements were determined using the method described in [36] using a reference target. A pitch angle was defined as 90°-ϕ to describe the angle formed by the optical axis with the x-y plane. The location r was defined as the distance from the center of the burner to the center of the camera lens.

Table 1. Orientation and location of the projection measurements.

Projection index	ϕ (degree)	θ (degree)	Pitch angle	r (cm)
1	74.88	–46.76	15.12	55.36
2	71.20	–10.40	18.80	42.20
3	71.76	45.40	18.24	42.80
4	74.84	86.40	15.16	55.28
5	71.20	90.80	18.80	42.20
6	74.60	121.60	15.40	54.60
7	71.04	153.04	18.96	42.00
8	74.60	176.40	15.40	54.60

Figure 7 shows a sample reconstruction using the projections tabulated above. In this reconstruction, the domain of interested (DOI) considered was a cylindrical region with a diameter of 67.5 mm and a height of 2.5 mm to encompass the flame (the flame has a diameter of ~61 mm and a thickness of ~1 mm). The DOI was descretized into 54 (x direction) × 54 (y direction) × 10 (z direction) voxels, resulting in a total of 29,160 voxels. Each voxel has a dimension of 1.25 mm in both the x and y directions and 0.25 mm in the z direction. The origin of the x-y-z coordinate is at the center of the burner as shown in Fig. 6.

Figure 7 shows the reconstructed flame at four different z positions. Panel (a) shows the reconstruction for the first layer right above the surface of the honeycomb (i.e., $0 < z < 0.25$ mm), and panel (b) through (d) the second, fourth, and eighth layers, respectively. Note that the results are displayed in layers simply for the sake of convenience and clarity. All algorithms in this work are implemented in 3D, and these algorithms solve the TC problem as a 3D problem. The results in this work were not obtained by stacking a series of 2D solutions layer by layer. The advantages of decomposing a 3D problem into a series of 2D problems

#175611 - $15.00 USD Received 5 Sep 2012; revised 1 Nov 2012; accepted 1 Jan 2013; published 13 Mar 2013

and solving them separately include simplicity and reduced computational requirements; however this approach also has disadvantages, both practical and fundamental. Practically, the experiments need to be designed to allow the conversion of 3D problems to 2D problems, resulting in complicated hardware, alignment, and loss of signal [20, 22]. A fundamental disadvantage involves consideration of regularization. When the problem is solved in 3D, regularization in all three directions can be considered simultaneously, which is difficult or even impossible when the problem is solved as a series of 2D problems.

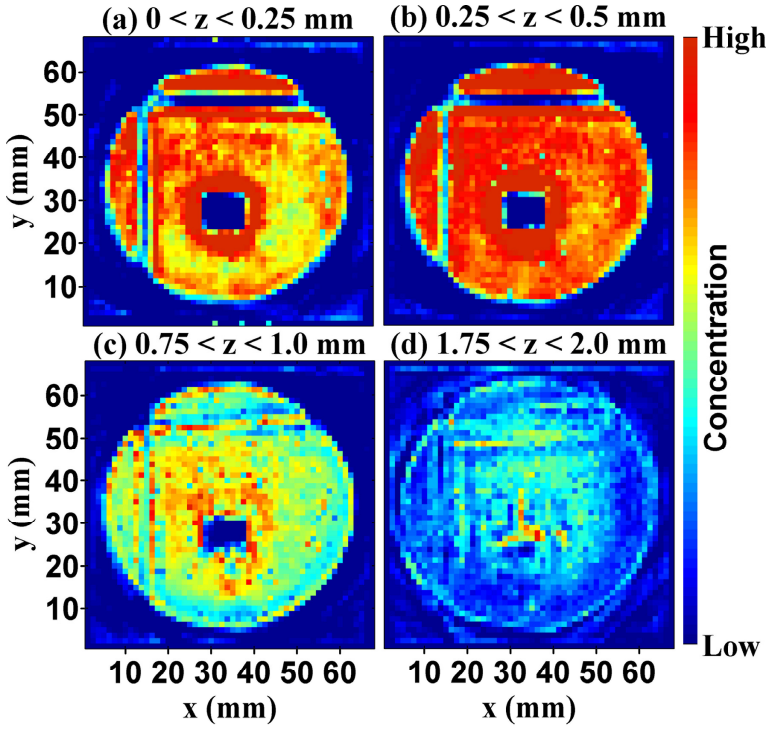

Fig. 7. Reconstructed flame at different z positions.

As shown in Fig. 7, the flame pattern created by the blockage was clearly resolved in the first two layers above the honeycomb. The TC technique successfully reconstructed the size and thickness of the flame, the size, shape, and location of the blocked regions. As the flame propagates further in the z direction, transport phenomena cause the pattern to be blurred, as suggested by the reconstruction at the fourth and eighth layers shown in panels (c) and (d), respectively.

Figure 8 analyzes the reconstruction fidelity quantitatively by examining the size of the blocked areas. Panel (a) through (d), respectively, shows the thickness of the blocked column and row, and the width and the height of the blocked rectangle of the flame pattern. These quantitative information were obtained by calculating the gradient of the reconstruction at each layer (e.g., those shown in Fig. 7) to determine locations of sharpest CH* concentration change, which were then subsequently used to calculate the size of the blocked areas as shown here in Fig. 8. At each layer, multiple values were obtained along the edge of the block region; and the square symbol represents the median of these values for a given layer and the error bar represents the std (standard deviation) of these values.

Figure 8 further elucidates the visual observations made in Fig. 7, illustrating the blurring of the flame pattern as it propagates along the z direction. For example, panel (a) shows the reconstructed thickness of the blocked column, created by blocking on column of the cells on the honeycomb. As mentioned in Section 5, these cells are square and have a size of $\Delta l = 1.25$

#175611 - $15.00 USD Received 5 Sep 2012; revised 1 Nov 2012; accepted 1 Jan 2013; published 13 Mar 2013

mm. The reconstructions yielded a median thickness of 1.25 mm for the first three layers, equal to the thickness of the blocked region, illustrating the limited blurring caused by transport. The std on these three layers were caused by a combination of four factors: the blurring due to transport, the non-uniformities caused by the blockage, measurement uncertainty, and the reconstruction artifacts. We argue that the first two factors are the major causes based on the simulations results reported in Fig. 2 and Fig. 5. Those results demonstrated that the RHybrid algorithm can reconstruct the thickness of a block column accurately under the measurement uncertainty expected here. Starting on the fourth layer, the difference between the reconstructed thickness and Δl gradually increases with the layer index, and so does the std. Such increasing difference and std suggest the more and more pronounced blurring of the flame pattern caused by the transport phenomena. Similar interpretations can be made for results shown in panels (b) to (d).

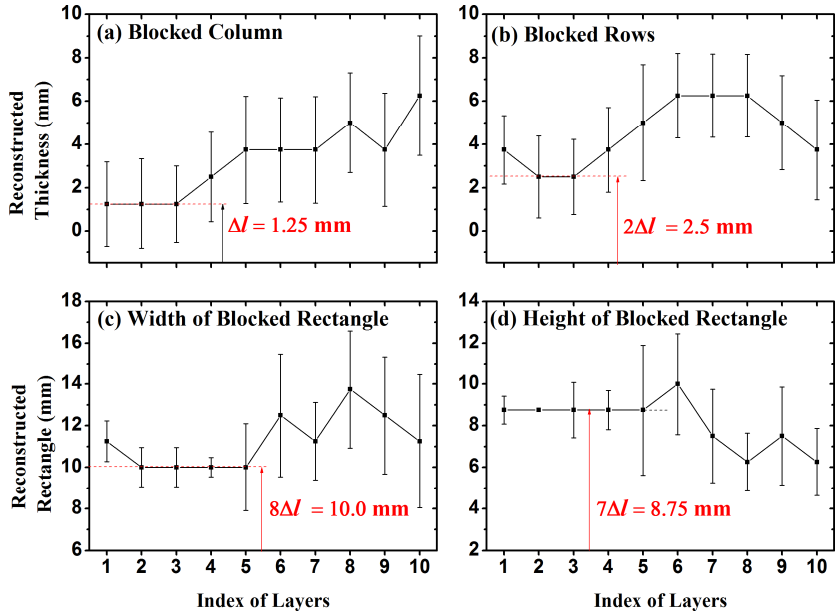

Fig. 8. The reconstructed size of blocked areas.

These results demonstrate the TC's ability to resolve flame structures (and also potentially transport physics). Here we focus on the spatial resolution of the TC technique. Sub-millimeter spatial resolution has been reported previously [23] for the TC technique based on a combination of theoretical analysis and experimental observations. The results in panel (a) of Fig. 8, in contrast, provide direct experimental data to demonstrate a spatial resolution on the order of 1.25 mm. Research work is underway to experimentally investigate the spatial resolution of the TC technique beyond 1.25 mm using the current experimental approach.

7. Advantages of random view orientation

This section discusses the effects of view orientations from which the projections are obtained. Our results suggest that for an unknown flame, it is advantageous to use random view orientations rather than coplanar orientations as typically used in the past. These findings are expected to illustrate the importance of optimizing view orientations, which is of both practical and fundamental relevance. Practically, combustion applications often have limited optical access and such access should be designed and used optimally. Fundamentally, it is desirable that projections obtained from different view orientations, especially when only a small number of view orientations are available, should provide complementary information, not redundant information.

#175611 - $15.00 USD Received 5 Sep 2012; revised 1 Nov 2012; accepted 1 Jan 2013; published 13 Mar 2013

Here, coplanar is defined as the TC configuration where the optical axes along which projections are obtained fall on the same plane. Such coplanar configuration seems to be natural, especially for a flame with open optical access. However, a coplanar configuration essentially poses a restriction on the view orientations, and may not provide the optimal information for the reconstruction. As a simple example, consider the flame pattern shown in panels (c) and (d) of Fig. 6. For this flame, views from the side (with a 0° pitch angle) largely provide redundant information (e.g., about the shape, size, and thickness of the flame). In contrast, a view from the top (with a 90° pitch angle) provides a wealth of key information about the flame structure: the shape, size, and location of the blocked areas besides the shape and size of the flame. As a result, two views, one from the side and another from the top, provide complimentary information for the reconstruction, which can be much more valuable than many coplanar views taken from the side. Therefore, generally, when the target flame is unknown, projections taken from random view orientations are statistically more likely to provide complementary information than coplanar view orientations. From a mathematical point of view, arbitrary view angles are more likely to provide projections that are more linearly independent from each other and reduce the ill-posedness of the problem.

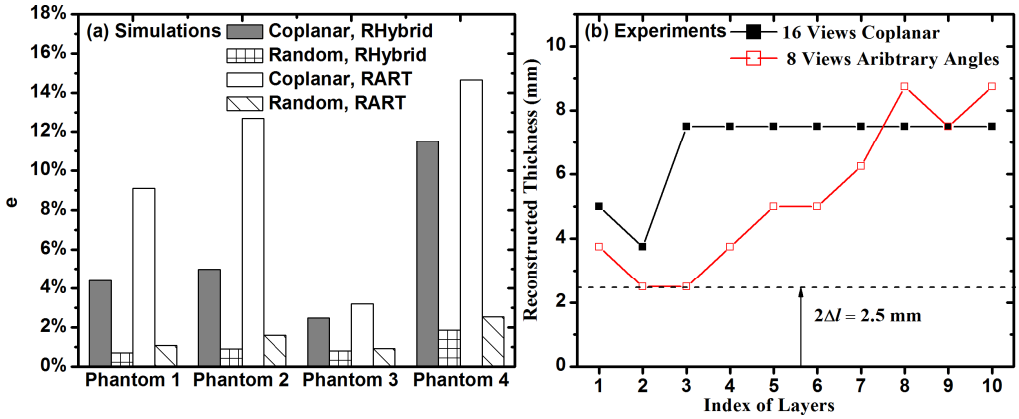

Fig. 9. Panel (a): comparison of e using coplanar and arbitrary view angles from numerical simulation. Panel (b): Reconstructed thickness using coplanar and non-coplanar view angles from experimental data.

The results shown in Fig. 9 confirm these intuitive arguments using both simulation (panel (a)) and experimental (panel (b)) studies. In panel (a), simulations were conducted using the RART and RHybrid algorithm to reconstruct the phantoms shown in Fig. 2 using eight projections, and 5% of artificial noise was added to the projections. Two sets of projections were used here: a set generated under the coplanar configuration and another set generated randomly. As can be seen, the reconstruction error from the coplanar configuration is consistently and substantially larger than that from the random view orientations. The reconstruction error from the coplanar configuration is also substantially larger than those reported in Fig. 3, which used randomly generated view orientations.

In panel (b), the experimentally-measured projections were used to reconstruct the flame patter by the RHybrid algorithm. We first used projections all obtained with a pitch angle of 0° (a coplanar configuration). Under such coplanar configuration, eight projections were insufficient to produce satisfactory reconstruction. Panel (b) shows the reconstructed thickness of the two blocked rows using sixteen coplanar projections. To elucidate the advantage of random orientations, we then used eight projections, randomly picked from a pool of projections measured at the orientations shown in Table 1 and also 0° degree pitch angle. As shown in panel (b), these eight projections provide complementary information to reconstruct the thickness significantly more accurately than the sixteen coplanar projections. Examination of other blocked areas reveals similar or more dramatic superiority of the randomly chosen orientations over the coplanar orientations.

#175611 - $15.00 USD Received 5 Sep 2012; revised 1 Nov 2012; accepted 1 Jan 2013; published 13 Mar 2013

Lastly, we make two comments before summarizing the paper. First, results in this work, both numerical and experimental, have all been obtained assuming no *a priori* information except that the sought distributions of the radicals are non-negative and bounded. When more *a priori* information is available, for example about the shape or geometry of the flame, it may no longer be optimal to use random orientations. Experiments should be designed to exploit such information. Second, we would like to iterate the value of the controlled flame patterns created in this work, in spite of the non-ideal features as mentioned earlier in Section 5. As seen from the results reported in Sections 6 and 7, these controlled patterns enable metrics which can be used to experimentally quantify critical aspects of the TC technique, such as the spatial resolution and reconstruction accuracy.

8. Summary

In summary, this work discusses a 3D combustion diagnostic based on tomographic chemiluminescence (TC). The TC techniques have several distinct advantages when compared to other non-intrusive laser diagnostics. The major contributions of this work are threefold. First, a hybrid algorithm is developed to solve the 3D TC problem. The algorithm is validated by extensive numerical simulations and experimental data. The hybrid algorithm outperformed other algorithms that we surveyed in terms of the reconstruction error, and was demonstrated to perform reconstruction with high fidelity using a limited number of view angles in the presence of noises. Second, a set of experiments were designed to both demonstrate the 3D TC technique, and also to examine its performance quantitatively. The experimental approach involves creating controlled flame patterns using a McKenna burner. These flame patterns enable quantifiable metrics to experimentally examine several critical aspects of the TC technique, such as the spatial resolution and reconstruction accuracy. The experimental results provide data that directly demonstrate a spatial resolution on the order of 1.25 mm and reconstruction with good fidelity with a limited number of projections. Third, based on the reconstruction algorithm and experimental results, we investigated the effects of the view orientations. The results suggested that for an unknown flame, it is better to use projections measured from random orientations than restricted orientations (e.g., coplanar orientations) because projections from random orientations are statistically more likely to provide complimentary information. Lastly, note that the second and third contributions are independent of the first one. We have examined our experimental data and the effects of view angles using different inversion algorithms, and the trend of the results obtained agreed with those obtained by the hybrid algorithm as reported.

#175611 - $15.00 USD Received 5 Sep 2012; revised 1 Nov 2012; accepted 1 Jan 2013; published 13 Mar 2013